Supporting Information

for

Supported Mn_3O_4 nanosystems for hydrogen production through ethanol photoreforming

Davide Barreca,[†] *Lorenzo Bigiani,*[‡] *Matteo Monai,*[§,‖] *Giorgio Carraro,*[‡] *Alberto Gasparotto,*[‡] *Cinzia Sada,*[⊥] *Sara Martí-Sanchez,*[#] *Albert Grau-Carbonell,*[#] *Jordi Arbiol,*[#,○] *Chiara Maccato,**[,‡] *and Paolo Fornasiero**[,‖]

[†] CNR-ICMATE and INSTM, Department of Chemical Sciences, Padova University, Via F. Marzolo, 1 - 35131 Padova, Italy

[‡] Department of Chemical Sciences, Padova University and INSTM, Via F. Marzolo, 1 - 35131 Padova, Italy

[§] Inorganic Chemistry and Catalysis Group - Debye Institute for Nanomaterials Science, Utrecht University, Universiteitsweg, 99 - 3584 CG Utrecht, The Netherlands

[‖] Department of Chemical and Pharmaceutical Sciences, ICCOM-CNR and INSTM, Trieste University, Via L. Giorgieri, 1 - 34127 Trieste, Italy

[⊥] Department of Physics and Astronomy, Padova University and INSTM, Via F. Marzolo, 8 - 35131 Padova, Italy

[#] Catalan Institute of Nanoscience and Nanotechnology (ICN2), CSIC and BIST, Bellaterra, 08193 Barcelona, Catalonia, Spain

[○] ICREA, Pg. Lluís Companys, 23 - 08010 Barcelona, Catalonia, Spain

* Corresponding authors; phone: +39-0498275234; e-mail: chiara.maccato@unipd.it (C.M.); phone: +39-0405583973; e-mail: pfornasiero@units.it (P.F.).

S-1. Synthesis

Mn_3O_4 nanodeposits were fabricated using a custom-built cold-wall CVD reactor.[1] $Mn(tfa)_2$•TMEDA (tfa = 1,1,1-trifluoro-2,4-pentanedionate; TMEDA = *N*,*N*,*N*',*N*'-tetramethylethylenediamine) was used as an innovative precursor, being an amenable alternative with respect to classical Mn β-diketonates typically adopted in vapor deposition processes.[2] The inherent advantages of such kind of molecular structures, along with the compound synthesis and chemico-physical characterization data, have recently been reported.[3-4] In CVD experiments, the compound was vaporized at 65°C, and transported into the reactor chamber by an electronic grade O_2 flow [rate = 100 standard cubic centimeters per minute (sccm)]. An independent O_2 flow (rate = 100 sccm) was separately introduced into the growth chamber. Connection gas lines were maintained at 105°C throughout each deposition process to avoid undesired precursor vapor condensation. The used Si(100) substrates (MEMC®, Merano, Italy; geometrical area = 1×1 cm^2) were cleaned prior to each deposition by washing in deionized water with sulphonic detergent, rinsing in deionized water and subsequently in 2-propanol, sonication in dicholometane and final rinsing in deionized water. At the end of each growth experiment, specimens were cooled down under flowing O_2 and subsequently used as-prepared, avoiding any thermal treatment to prevent the thermally-activated transformation of Mn_3O_4 into other Mn oxides.[5-6]

Functionalization of Mn_3O_4 samples with gold nanoparticles was carried out by means of a custom-built two-electrode radio frequency (RF) plasmochemical reactor (ν = 13.56 MHz),[7] using electronic grade Ar as plasma source (flow rate = 10 sccm). A gold target (BALTEC AG; thickness = 0.1 mm; purity = 99.99 %) was fixed on the RF electrode, and supported Mn_3O_4 specimens were mounted on a second grounded electrode (T = 60°C). Basing on a preliminary screening of processing parameters, the use of RF-powers and sputtering times higher than the present ones (5 W and 30 min, respectively) was intentionally avoided, in order to prevent the

fabrication of compact systems with an excessive gold loading and a reduced active area, that could have a detrimental influence on material functional performances.[8]

S-2. Characterization

S-2.1. Atomic force microscopy (AFM)

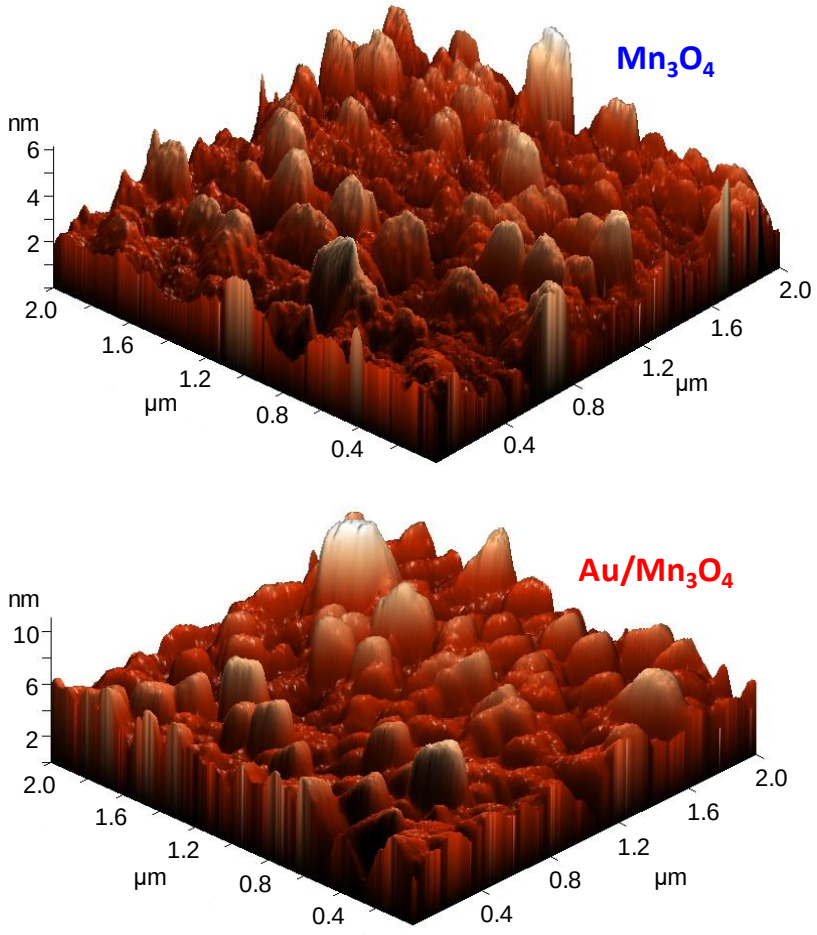

Figure S1. 2 μm × 2 μm AFM micrographs for Mn_3O_4 and Au/Mn_3O_4 specimens supported on Si(100).

S-2.2. X-ray diffraction (XRD)

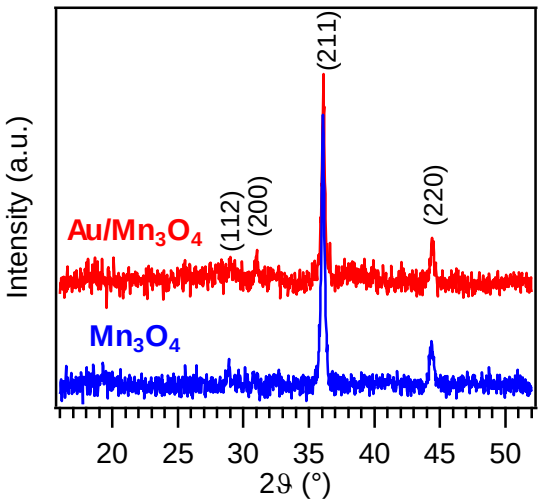

Figure S2. GIXRD patterns of Mn_3O_4 and Au/Mn_3O_4 samples collected at an incidence angle of 1.0°.

S-2.3. Transmission electron microscopy (TEM) and energy dispersive X-ray spectroscopy (EDXS)

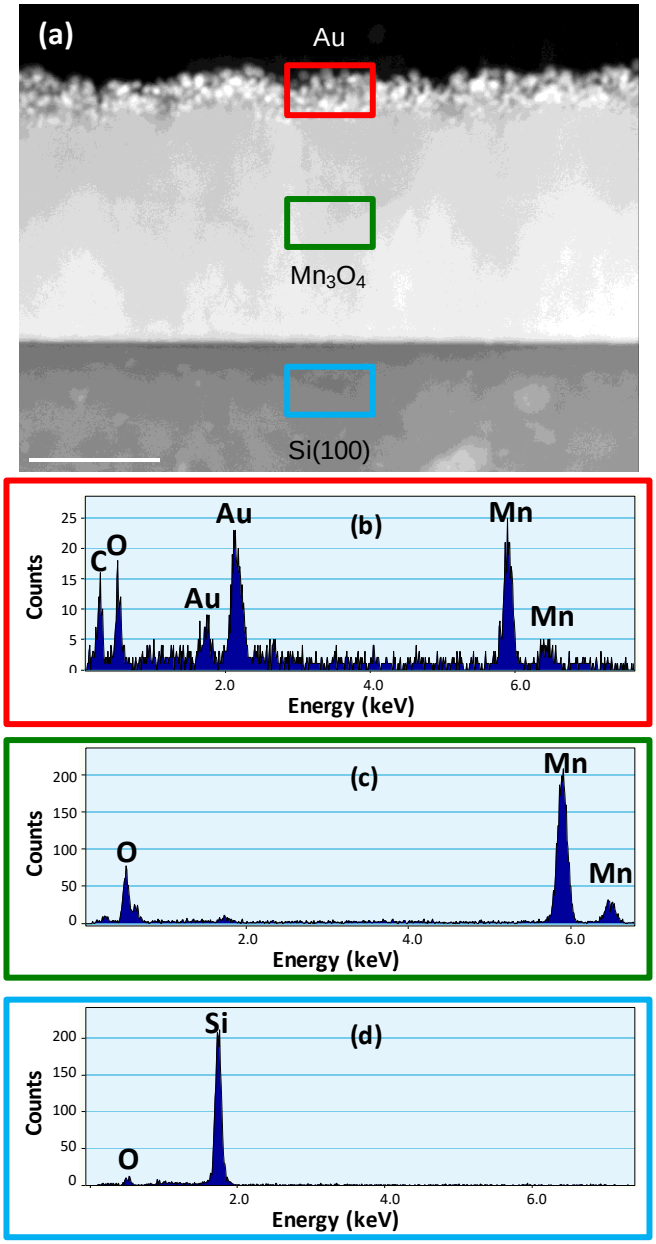

Figure S3. (a) HAADF-STEM micrograph of an Au/Mn_3O_4 sample. *Z*-contrast allows to differentiate the Si(100) substrate, the Mn_3O_4 region and the near-surface one. The coloured boxes correspond to EDXS spectra obtained: (b) in the outermost region, where Au nanoparticles are mainly concentrated. The presence of carbon in the outermost sample region arises from the glue used for the cross-sectional preparation process; (c) in the Mn_3O_4 deposit; (d) in the Si(100) substrate, where a minor O signal is also observed.

S-2.4. X-ray photoelectron spectroscopy (XPS)

The first step in XPS spectral analysis consists in the identification of all photopeaks related to the different elements contained in the target samples. Nevertheless, in some cases the overlaps of photoelectron peaks originating from different elements may complicate the analytical process. This was the case of Au/Mn_3O_4 samples, in which the most intense Mn2p and Au4f signals were overlapping with the $Au4p_{1/2}$ spin orbit component and the Mn3s peaks, respectively, because of the very similar binding energy (BE) values.[9-10] In the case of Au, quantitative analyses can be carried out using the interference-free $Au4d_{5/2}$ line.[11] Regarding manganese, the Mn3p peak could, in principle, be utilized, but the appreciable BE difference with the O1s peak would imply the analysis of photoelectrons with different escape depths, affecting thus the O/Mn ratio.[12]

To overcome the above problem and quantify both Au and Mn atomic percentages (at. %) in the case of Au/Mn_3O_4 systems, the following procedure was adopted, in line with a previous study.[13] The $Au4p_{1/2}/Au4d_{5/2}$ area ratio can be obtained by the corresponding sensitivity factor ratio, $S(Au4p_{1/2})/S(Au4d_{5/2})$, according to the following relation:

$$A(Au4p_{1/2})/A(Au4d_{5/2}) = S(Au4p_{1/2})/S(Au4d_{5/2}) \quad \text{(S1)}$$

Since $Au4d_{5/2}$ area can be directly measured from the spectra, $Au4p_{1/2}$ area can be estimated provided that the $S(Au4p_{1/2})/S(Au4d_{5/2})$ ratio[14] is known. Subsequently, Mn2p area [A(Mn2p)] can be computed by the area difference of the [A(Mn2p) + $A(Au4p_{1/2})$] and $A(Au4p_{1/2})$ signals, and used for the calculations of atomic percentage (at. %) values according to the relation:[9]

$$C_i = 100\frac{A_i}{S_i}\left(\sum_j \frac{A_j}{S_j}\right)^{-1} \quad \text{(S2)}$$

where C_i, A_i and S_i represent the at. % value of the i element, the area of the corresponding photopeak and the sensitivity factor, respectively.

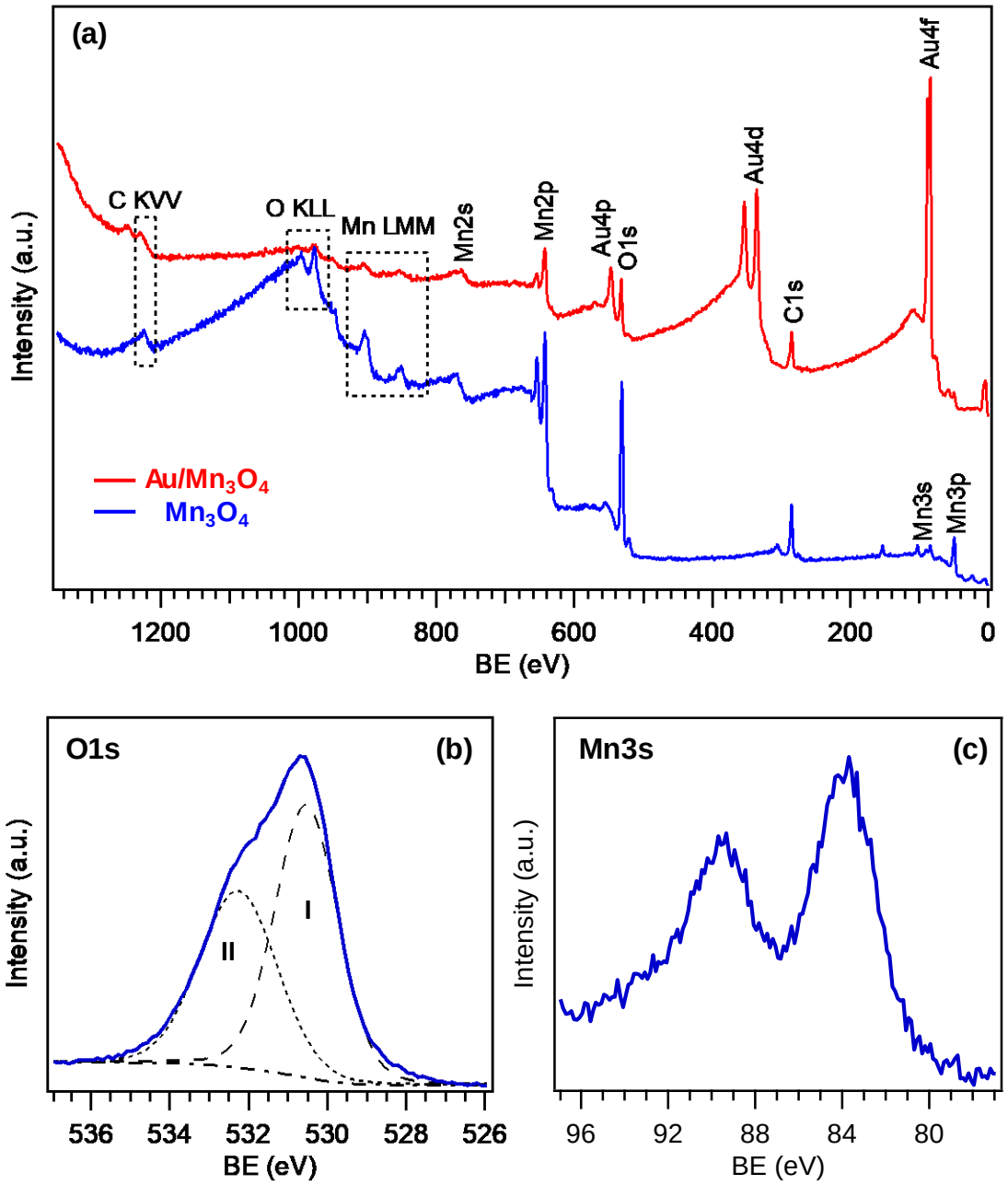

Figure S4. (a) Surface XPS wide-scan spectra for Mn_3O_4 and Au/Mn_3O_4 nanodeposits. The O1s (b) and Mn3s (c) photopeaks for a Mn_3O_4 sample are also displayed. In the case of O1s, the two components resulting from peak fitting are also displayed.

S-2.5. Photoreforming experiments for H_2 production

Photoreforming experiments were carried out without the application of any external bias, using a previously described experimental apparatus.[15] Illumination was performed using a solar simulator (LOT-Oriel) equipped with a 150 W Xe lamp, using an Atmospheric Edge filter in order to exclude the contribution of UV photons (λ < 300 nm). The light intensity for simulated sunlight experiments, measured by a radiometer, was ≈25 and ≈180 mW cm^{-2} in the 250-400 nm and 400-1000 nm spectral ranges, respectively. All tests were performed with the photoreactor immersed in a thermostatic bath at 25°C. Samples were immersed in a ethanol:water 1:1 volume mixture and the system was flushed with Ar in the dark until air was no longer detected by gas chromatrography (GC) analysis. During illumination, the evolved hydrogen was removed from the solution by an Ar flow (15 mL min^{-1}) and detected on-line by an Agilent 7890 GC apparatus, equipped with a 10 way-two loop injection valve. H_2 analysis was performed by means of a Carboxen 1010 PLOT column (Supelco, 30 m × 0.53 mm ID, 30 μm film) connected to a Thermal Conductivity Detector (TCD), using electronic grade Ar as carrier gas. The yield data were normalized for the geometrical area of the target samples (see above). Preliminary control tests evidenced the absence of any appreciable H_2 photogeneration in the dark and/or in the absence of the photocatalysts.

Solar-to-Fuel Efficiency (SFE) values were calculated using the following equation:[16-18]

$$SFE = \frac{\Delta E}{S} \times 100 \qquad \text{(S3)}$$

where ΔE corresponds to the amount of photoproduced H_2 (mol s^{-1} cm^{-2}) multiplied by hydrogen combustion enthalpy (285.8 kJ mol^{-1}), and S represents the total incident solar irradiance (W cm^{-2}).

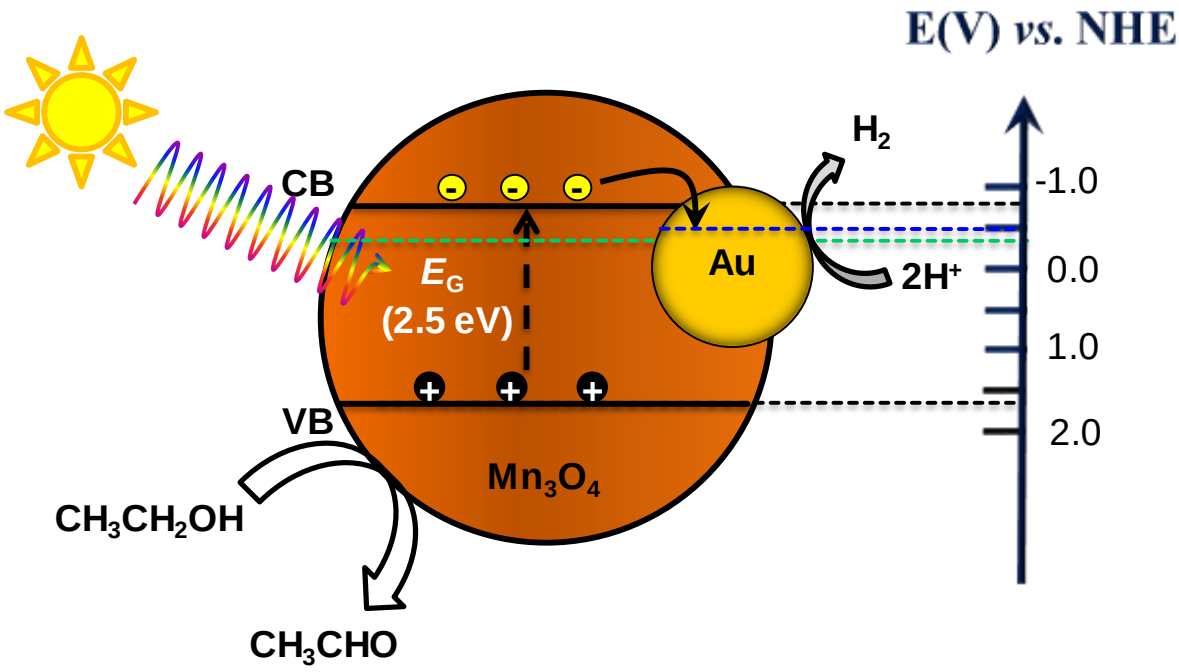

Figure S5. Sketch of the photoactivity enhancement mechanism for Au/Mn_3O_4 nanosystems under simulated sunlight. CB, VB and E_G: conduction, valence band edges and energy gap of Mn_3O_4.[3,19] The redox potential of the H^+/H_2 couple at pH = 7.0, corresponding to the presently adopted conditions, is marked by a horizontal green dashed line. The blue dashed line indicates the Fermi level position for gold nanoparticles.[20]

The scheme in Figure S5 is a simplified representation of ethanol photoreforming mechanism. As a matter of fact, the oxidation of ethanol to acetaldehyde can proceed either by direct reaction of ethanol with the holes photogenerated in Mn_3O_4 (h^+):

$$CH_3CH_2OH + 2h^+ \rightarrow CH_3CHO + 2H^+ \quad \text{(S4)}$$

or by ethanol dissociative chemisorption on Mn_3O_4, forming ethoxy radical species that are subsequently oxidized to acetaldehyde:[21-22]

$$CH_3CH_2O–H + Mn_{(s)}–O_{(s)} \rightarrow CH_3CH_2O–Mn_{(s)} + H–O_{(s)} \quad \text{(S5)}$$

$$CH_3CH_2O^{\cdot} + h^+ \rightarrow CH_3CHO + H^+ \quad \text{(S6)}$$

where $Mn_{(s)}$ and $O_{(s)}$ are surface Mn and O atoms in Mn_3O_4. Alternatively, even a process mediated by H_2O can occur, in which oxidation is carried out by hydroxyl radical species, formed by reaction of water with photogenerated holes:

$$H_2O + h^+ \rightarrow H^+ + {}^{\cdot}OH \quad \text{(S7)}$$

$$CH_3CH_2OH + {}^{\cdot}OH + h^+ \rightarrow CH_3CHO + H_2O + H^+ \quad \text{(S8)}$$

The produced H^+ ions can then lead to H_2 formation:

$$2H^+ + 2e^- \rightarrow H_{2(g)} \quad \text{(S9)}$$

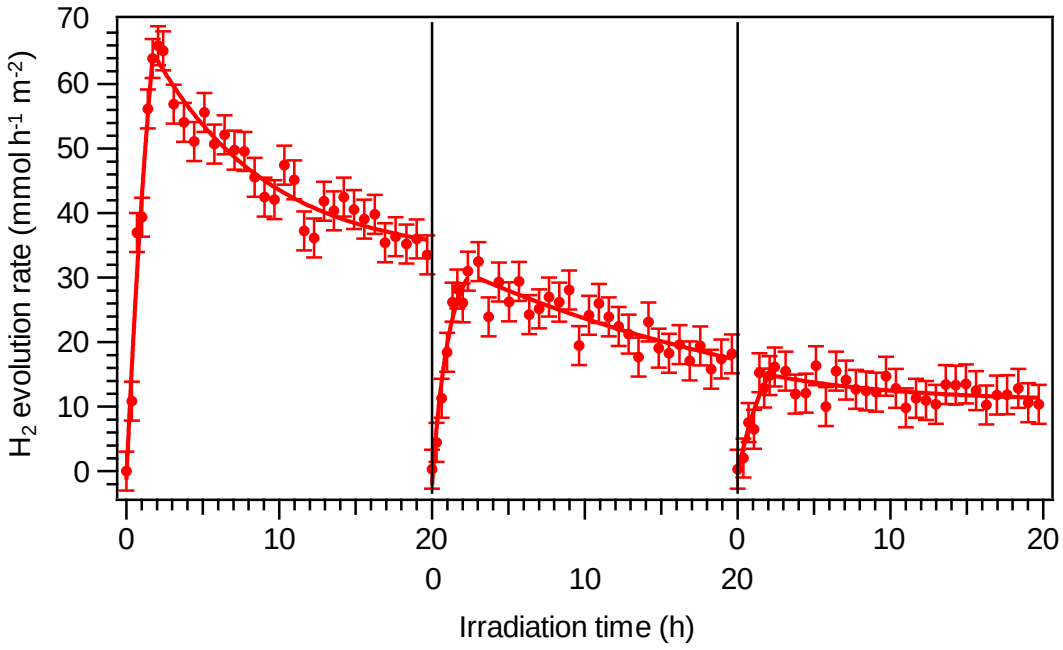

Figure S6. H_2 production rates per unit area in recyclability tests over Au/Mn_3O_4 in photoreforming of ethanol/water solutions upon simulated sunlight irradiation. Between two consecutive cycles (vertical bars in the figure), samples were rinsed with ethanol and the solution was replaced. The catalytic run was repeated as described in the experimental details.

S-2.6. Characterization of Au/Mn_3O_4 catalysts after use

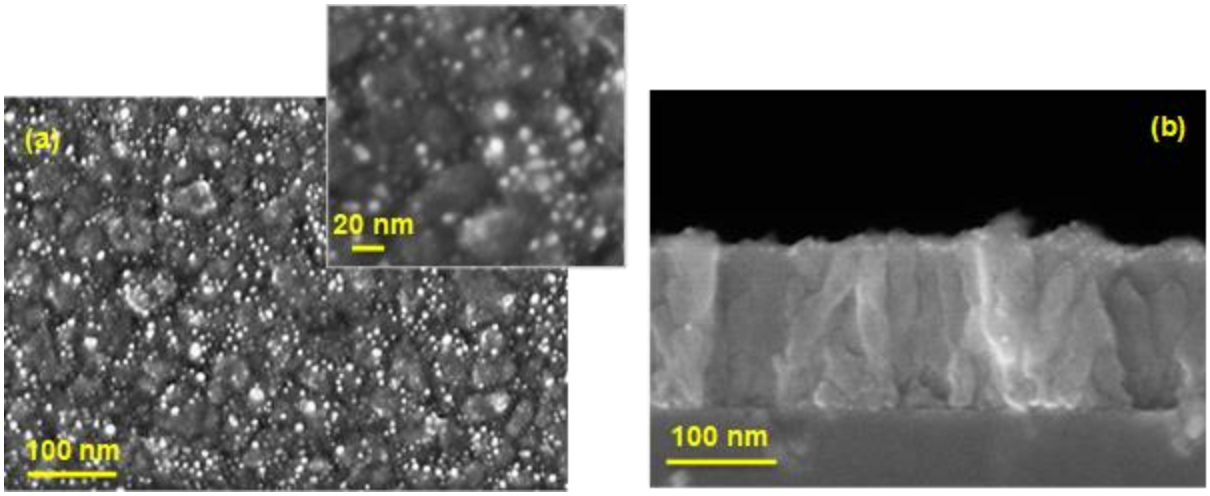

Figure S7. Characterization of an Au/Mn_3O_4 specimen after photoreforming experiments for hydrogen production. Plane-view (a) and cross-sectional (b) FE-SEM images.

References

(1) Barreca, D.; Gasparotto, A.; Maragno, C.; Tondello, E.; Sada, C. CVD of Nanophasic (Zn,Cd)S Thin Films: From Multi-Layers to Solid Solutions. *Chem. Vap. Deposition* **2004**, *10*, 229-236.

(2) Mattelaer, F.; Bosserez, T.; Ronge, J.; Martens, J. A.; Dendooven, J.; Detavernier, C. Manganese Oxide Films with Controlled Oxidation State for Water Splitting Devices Through a Combination of Atomic Layer Deposition and Post-Deposition Annealing. *RSC Adv.* **2016**, *6*, 98337-98343.

(3) Maccato, C.; Bigiani, L.; Carraro, G.; Gasparotto, A.; Seraglia, R.; Kim, J.; Devi, A.; Tabacchi, G.; Fois, E.; Pace, G.; Di Noto, V.; Barreca, D. Molecular Engineering of Mn^{II} Diamine Diketonate Precursors for the Vapor Deposition of Manganese Oxide Nanostructures. *Chem. Eur. J.* **2017**, *23*, 17954-17963.

(4) Barreca, D.; Carraro, G.; Fois, E.; Gasparotto, A.; Gri, F.; Seraglia, R.; Wilken, M.; Venzo, A.; Devi, A.; Tabacchi, G.; Maccato, C. Manganese(II) Molecular Sources for Plasma-Assisted CVD of Mn Oxides and Fluorides: From Precursors to Growth Process. *J. Phys. Chem. C* **2018**, *122*, 1367-1375.

(5) Liu, G. Y.; Hall, J.; Nasiri, N.; Gengenbach, T.; Spiccia, L.; Cheah, M. H.; Tricoli, A. Scalable Synthesis of Efficient Water Oxidation Catalysts: Insights into the Activity of Flame-Made Manganese Oxide Nanocrystals. *ChemSusChem* **2015**, *8*, 4162-4171.

(6) Jeon, H. S.; Ahn, S. J.; Jee, M. S.; Yoon, S. S.; Hwang, Y. J.; Min, B. K. Water Oxidation by Manganese Oxide Electrocatalytic Films Synthesized by Chemical Solution Deposition Method. *J. Electrochem. Soc.* **2016**, *163*, F3113-F3118.

(7) Barreca, D.; Gasparotto, A.; Tondello, E.; Sada, C.; Polizzi, S.; Benedetti, A. Nucleation and Growth of Nanophasic CeO_2 Thin Films by Plasma-Enhanced CVD. *Chem. Vap. Deposition* **2003**, *9*, 199-206.

(8) Carraro, G.; Maccato, C.; Gasparotto, A.; Warwick, M. E. A.; Sada, C.; Turner, S.; Bazzo, A.; Andreu, T.; Pliekhova, O.; Korte, D.; Lavrenčič Štangar, U.; Van Tendeloo, G.; Morante, J. R.; Barreca, D. Hematite-Based Nanocomposites for Light-Activated Applications: Synergistic Role of TiO_2 and Au Introduction. *Sol. Energy Mater. Sol. Cells* **2017**, *159*, 456-466.

(9) Moulder, J. F.; Stickle, W. F.; Sobol, P. E.; Bomben, K. D., *Handbook of X-ray Photoelectron Spectroscopy*. Perkin Elmer Corperation, Eden Prairie, MN, USA: 1992.

(10) http://srdata.nist.gov/xps.

(11) Frydendal, R.; Seitz, L. C.; Sokaras, D.; Weng, T. C.; Nordlund, D.; Chorkendorff, I.; Stephens, I. E. L.; Jaramillo, T. F. Operando Investigation of Au-MnO_x Thin Films with Improved Activity for the Oxygen Evolution Reaction. *Electrochim. Acta* **2017**, *230*, 22-28.

(12) Briggs, D.; Seah, M. P., *Practical Surface Analysis: Auger and X-ray Photoelectron Spectroscopy*. John Wiley & Sons: New York, 2nd ed.: 1990.

(13) Canevali, C.; Scotti, R.; Vedda, A.; Mattoni, M.; Morazzoni, F.; Armelao, L.; Barreca, D.; Bottaro, G. Composition/Structure Relationships in Monolithic Borophosphosilicate Glasses Obtained by the Sol−Gel Route. *Chem. Mater.* **2004**, *16*, 315-320.

(14) *Multi-Technique ESCA Operators Reference Manual*, Version 5.2 (Perkin-Elmer, Eden Prairie, MN, 1994), Part No. 625411, Rev. C.

(15) Carraro, G.; Maccato, C.; Gasparotto, A.; Montini, T.; Turner, S.; Lebedev, O. I.; Gombac, V.; Adami, G.; Van Tendeloo, G.; Barreca, D.; Fornasiero, P. Enhanced Hydrogen Production by Photoreforming of Renewable Oxygenates through Nanostructured Fe_2O_3 Polymorphs. *Adv. Funct. Mater.* **2014**, *24*, 372-378.

(16) Barreca, D.; Carraro, G.; Gasparotto, A.; Maccato, C.; Warwick, M. E. A.; Toniato, E.; Gombac, V.; Sada, C.; Turner, S.; Van Tendeloo, G.; Fornasiero, P. Iron–Titanium Oxide Nanocomposites Functionalized with Gold Particles: From Design to Solar Hydrogen Production. *Adv. Mater. Interfaces* **2016**, *3*, 1600348.

(17) Carraro, G.; Barreca, D.; Bekermann, D.; Montini, T.; Gasparotto, A.; Gombac, V.; Maccato, C.; Fornasiero, P. Supported F-Doped α-Fe_2O_3 Nanomaterials: Synthesis, Characterization and Photo-Assisted H_2 Production. *J. Nanosci. Nanotechnol.* **2013**, *13*, 4962-4968.

(18) Artioli, G. A.; Mancini, A.; Barbieri, V. R.; Quattrini, M. C.; Quartarone, E.; Mozzati, M. C.; Drera, G.; Sangaletti, L.; Gombac, V.; Fornasiero, P.; Malavasi, L. Correlation between Deposition Parameters and Hydrogen Production in CuO Nanostructured Thin Films. *Langmuir* **2016**, *32*, 1510-1520.

(19) Li, N.; Tian, Y.; Zhao, J.; Zhang, J.; Zhang, J.; Zuo, W.; Ding, Y. Efficient Removal of Chromium from Water by Mn_3O_4@ZnO/Mn_3O_4 Composite under Simulated Sunlight Irradiation: Synergy of Photocatalytic Reduction and Adsorption. *Appl. Catal., B* **2017**, *214*, 126-136.

(20) Kiyonaga, T.; Fujii, M.; Akita, T.; Kobayashi, H.; Tada, H. Size-Dependence of Fermi Energy of Gold Nanoparticles Loaded on Titanium(iv) Dioxide at Photostationary State. *Phys. Chem. Chem. Phys.* **2008**, *10*, 6553-6561.

(21) Shimura, K.; Yoshida, H. Heterogeneous Photocatalytic Hydrogen Production from Water and Biomass Derivatives. *Energy Environ. Sci.* **2011**, *4*, 2467-2481.

(22) Strataki, N.; Bekiari, V.; Kondarides, D. I.; Lianos, P. Hydrogen Production by Photocatalytic Alcohol Reforming Employing Highly Efficient Nanocrystalline Titania Films. *Appl. Catal., B* **2007**, *77*, 184-189.